

# Numerical framework for aerodynamic and aeroacoustics of bio-inspired UAV blades

Robbie WILKINS\* and Abdessalem BOUFERROUK\*†

\* University of the West of England, BS16 1QY BRISTOL, United Kingdom

† Corresponding Author: [abdessalem.bouferrouk@uwe.ac.uk](mailto:abdessalem.bouferrouk@uwe.ac.uk)

## Abstract

With the aim to understand and control the noise from UAVs, this work presents a numerical framework for a small-scale rotor blade with a bio-inspired finlet design. The simulation framework employs Direct Eddy Simulation (DES) for fluid flow and Ffowcs-Williams-Hawkings (FW-H) acoustic analogy for far-field acoustic data. Aerodynamic and aero-acoustic validation of the framework for a hovering case is achieved using a single DJI-9450 rotor blade. Good agreement is shown against experimental and numerical published data. To allow for ease of modelling of finlets on the blade, the original blade twist was modified from mid to tip, creating an ‘idealised’ blade. The time-averaged thrust coefficient of the baseline idealised blade is found to be almost the same as that obtained with finlets, indicating a negligible effect on the blade aerodynamics due to finlets. Although no reliable acoustic data could be obtained with finlet design due to computational limitations, close observation of the flow behaviour reveals some interesting patterns. There is a reduced turbulent kinetic energy (TKE) due to finlets, as well as the occurrence of some discrete turbulent blobs that seem to travel above the finlets. These phenomena could indicate either turbulence lifting of smaller-scale eddies or turbulence channelling by the finlets, both of which are known to reduce noise. The presented framework with initial finlet design and numerical testing can be used for the purpose of future noise-optimisation studies.

## 1. Introduction

The use of UAVs has grown in recent years, with a general strive towards optimisation and efficiency gains leading the front [1-2]. One of the major limiting factors to this optimised future, however, is the noise generated particularly in urban environments, causing significant annoyance. Noting the growing trend of UAV utilisation, and aiming for UAV acceptance within the population, NASA [3] suggested high-level goals to be addressed, where the focus should be towards measured and simulated acoustic data acquisition, for predictive model and optimisation research purposes.

UAV noise, primarily aerofoil self-noise, is generally split into tonal (discrete frequency) noise and broadband (general frequency coverage) noise [4], caused by the interaction of the blade surfaces with the unsteady flow in the form of turbulence. Tonal noise is divided into deterministic components of ‘thickness’ and ‘loading’ noise, and ‘blade-vortex interaction’ (BVI) noise [5]. Broadband noise contains the non-deterministic ‘loading’ noise components, categorised into ‘turbulence-ingestion noise’, ‘blade-wake interaction’ (BWI) noise, and ‘blade self-noise’ [6]. Numerically predicting these phenomena generally involves decoupling acoustic pressure fluctuations and aerodynamic pressure fluctuations, due to acoustic pressure fluctuations occurring orders of magnitude lower than aerodynamic pressure fluctuations, and numerical methods being incapable of coping with the higher-order accuracy required. Usually, the FW-H analogy is used, derived for walls/ moving bodies enclosed within a permeable or porous source surface [7]. Much attention, both numerically and experimentally, has been paid to optimisation for noise control purposes through passively reducing the unsteady turbulent flow, including serrated trailing-edge (STE) aerofoil and flat plate designs [8-20], whale fin-wave inspired blades [21], serrated-leading-edge (SLE) aerofoil, flat plate, and propeller designs [22-25], with further systems reviewed in [26], including BL tripping systems, porous metal inserts, and/or a combination of all mentioned. Bio-inspired flat plate, aerofoil, rotor, and propeller systems have also become a popular solution [27-29]. Bio-inspired designs have demonstrated significant noise-reductions over conventional designs both numerically and experimentally and they are being considered as viable noise reduction technologies.

Upstream surface treatments, such as finlets (tiny fins) have demonstrated significant reductions in aerofoil and flat plate TE noise [30-33, 36-37] and will be studied in this paper. Finlets are inspired by the canopy structures formed by the hairs of owl feathers. The reduced noise is attributed to turbulent kinetic energy ‘channelling’ and ‘lifting’ away from the TE for the smaller-scale eddies, leading to a reduced edge scattering, and lowered power spectral density (PSD) for the low-mid or mid-high frequencies in the TE region. While previous work [36-37] presented the

DOI: ADD DOINUMBER HERE

effectiveness of upstream surface treatments on the NACA0012 aerofoil, and further works using finlet ‘rails’ and ‘fences’ [34-35, 38-39] have been conducted for flat plates and aerofoils, application of this to the field of small rotor blades for UAV or propeller use has not been explored. The present work proposes a numerical framework in which the finlet design is considered and applied to an idealized DJI-9450 UAV blade profile, with aerodynamic and aeroacoustics comparisons drawn, and initial finlet blade design results presented.

## 2. Methodology

### 2.1 UAV Case Definition

A drone is chosen for the work to: i) provide a baseline for numerical validation, ii) to allow for further design-optimisation, and iii) to be commercially available. The DJI-9450 rotor blade (used on the DJI-Phantom 3 UAV) forms the baseline for the current work. Figure 1 displays the two-bladed rotor that is modelled. GrabCAD was used to obtain the rotor geometry in .STEP file format [40]. The UAV definition and operating conditions are presented in table 1 (based on general drone use and having validation data sets), while table 2 lists blade dimensions.



Figure 1- DJI-9450 single- rotor configuration CAD

Table 1- UAV Case Definition & Operating Conditions

| Parameter            | Choice                      | Unit |
|----------------------|-----------------------------|------|
| Drone                | DJI-Phantom 3/Phantom 3 Pro | n/a  |
| Rotor                | DJI-9450                    | n/a  |
| RPM                  | 6000                        | -    |
| Operation phase      | Hovering                    | n/a  |
| Operating conditions | Sea level                   | n/a  |

Table 2- DJI-9450 rotor blade dimensions

| Parameter       | Nomenclature | Dimension [m] |
|-----------------|--------------|---------------|
| Average Chord   | $C_{avg}$    | 0.025         |
| Rotor diameter  | $D$          | 0.239         |
| Rotor tip-chord | $C_{tip}$    | 0.01          |

### 2.2 Computational Set-up

Following the numerical work in [41], similar computational domain and corresponding BCs are chosen. Figure 2 shows the computational domain. The ‘bullet-shaped’ domain spans a radius of  $10 \times L$  in the rotor-plane,  $5 \times L$  in the upstream spherical extent, and  $20 \times L$  downstream of the rotor-plane. Within this *static* extent, a  $1.1 \times L$  diameter cylindrical *rotating* domain encapsulates the rotor, with  $0.2 \times L$  above and below the upper- and lower-rotor surface limits. The BCs chosen simulate hovering, with an outlet directly downstream of the rotor-plane, in the direction of the jet-stream, and inlets surrounding all-but the outlet, where no jet-stream would occur. Following [41], the  $k - \omega$  SST turbulence model is utilised by default. To accurately model the boundary layer, 20 prism layers discretized a  $0.001m$  height over the rotor surface, corresponding to a wall-normal viscous unit resolution of  $y^+ < 5$ , for all simulations. Outside of the prism layer region, the rotational and static domain grid sizing is altered, according to the desired resolution during mesh independence studies. The solution procedure follows an initialization through steady-

DOI: ADD DOINUMBER HERE

state conditions, employing the ‘moving reference frame’ model for the rotational domain, with a ‘sliding mesh zone’ later utilised for the rotational domain of the transient solution.

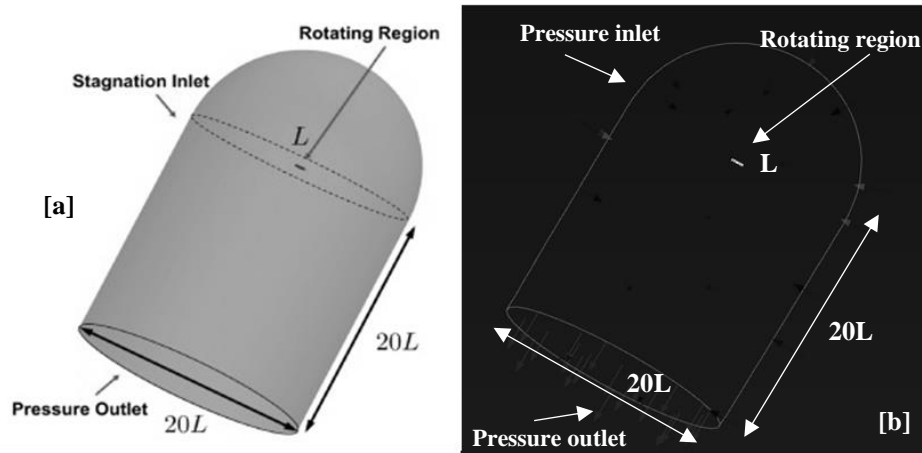


Figure 2- Computational domain of [41] (a), and the present computational domain (b)

The procedure is suggested in [42] to reduce the computational time of a case with zone translational or rotational velocities. For solution stability, the steady and unsteady solutions use different methods and controls, as suggested in [42], and listed for steady and transient solvers in table 3. If the method, control, or relaxation is not mentioned, the default within ANSYS Fluent is employed. The governing equations and averaged thrust coefficient  $C_T$  residuals are set to  $1e-5$  for steady-state, and unsteady-state, however for each individual timestep, as opposed to the whole solution, with a maximum of 20 iterations per timestep completed. Table 5 lists the unsteady time settings used within the present work. The timestep size corresponds to  $3^\circ$  rotation per timestep, or 120 timesteps per full rotation. Therefore, 0.01s of physical time pass per rotation, or a rotational frequency of 100Hz, and an incompressible Reynolds number of  $1.25e+5$ . For the flow-field, 3600 timesteps, or 0.3s of run time is used for simulations, unless stated otherwise.

Table 3- Steady-state and transient solver settings, controls, & relaxations

| Criteria                      | Steady state          | Transient run         |
|-------------------------------|-----------------------|-----------------------|
| Pressure-velocity formulation | SIMPLE                | Coupled               |
| Velocity scheme               | 2 <sup>nd</sup> Order | 2 <sup>nd</sup> Order |
| Pressure scheme               | PRESTO!               | 2 <sup>nd</sup> Order |
| Momentum under-relaxation     | 0.5                   | 0.7                   |
| Pressure under-relaxation     | 0.7                   | 0.7                   |

Table 4- Transient time-settings

| Criteria                 | Nomenclature   | Selection | Unit    |
|--------------------------|----------------|-----------|---------|
| Timestep size            | $\Delta t$     | $8.33e-5$ | Seconds |
| Timesteps per rotation   | $\Delta t/rot$ | 120       | n/a     |
| Timesteps                | n/a            | 3600      | n/a     |
| 1-rotation physical time | n/a            | 0.01      | Seconds |
| Rotational frequency     | $f_{rot}$      | 100       | Hertz   |

Acoustic modelling and related parameters (listed in table 6) chosen for the present work are inspired by previous works [41,43-44]. Once acoustic source data is acquired, the unfiltered signal is processed through Fast Fourier Transform (FFT), with a Hamming window applied.

Table 5- Default acoustic settings & quantities

| Criteria            | Nomenclature | Selection | Unit       |
|---------------------|--------------|-----------|------------|
| Flow periods        | n/a          | 0-30      | n/a        |
| Source-data periods | n/a          | 30-50     | n/a        |
| Reference pressure  | $atm$        | 1         | Atmosphere |

DOI: ADD DOINUMBER HERE

|                          |      |        |               |
|--------------------------|------|--------|---------------|
| Reference sound pressure | $Pa$ | $2e-5$ | Pascal        |
| Speed of sound           | $a$  | 340    | Meters/second |

### 3. Model Validation

#### 3.1 Grid independence

The focus of grid refinements is the rotational domain, to capture rotor-induced-thrust. Capturing key flow physics such as rotor-wake interaction, and how this affects blade loading, and wake-vortex interactions, and thus acoustic wave propagation and attenuation is essential. To achieve this, a wake-zone is discretized immediately downstream of the rotational domain, containing  $\sim 1\,000\,000$  elements, with the rotor at the centre of the  $0.625 \times L$  radius cylinder, and a downstream distance from the rotor of  $2.5 \times L$ . The base grid is depicted in figure 3. To judge grid convergence, the thrust coefficient  $C_T$  is calculated (Equation 1), with averaged values across the final three rotations being taken, corresponding to 0.03s in flow time, while flow features are observed for the qualitative investigation.

$$C_T = \frac{T}{\rho A (\Omega R)^2} \quad (1)$$

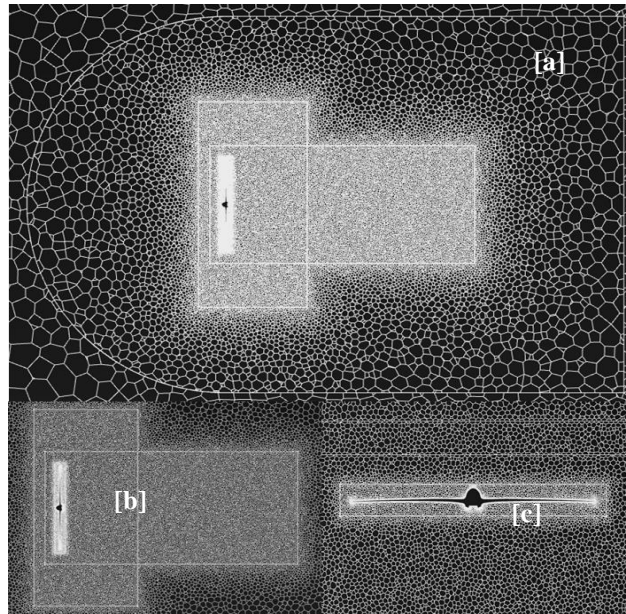


Figure 3- Baseline single-rotor grid with the far-field (a), near-field (b), and rotational domain (c) depicted.

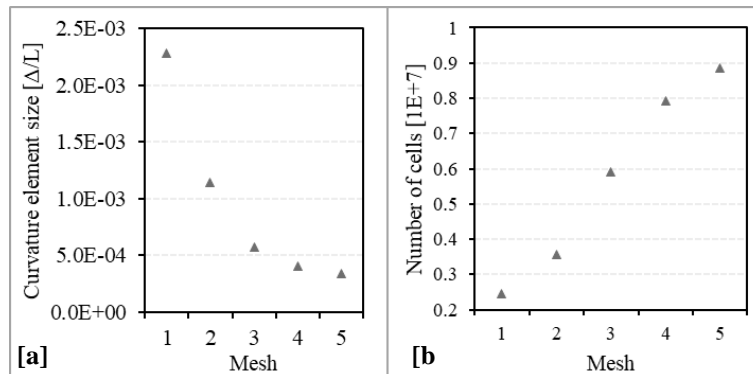


Figure 4- Curvature sizing-function study with normalized sizing's (a), and resulting cell-counts (b)

To accurately capture and discretize the blade curvature for capturing the high-gradient flow physics about the LE and TE of the blade, the blade face-curvature function is altered. Figure 4 (a) displays the sizing applied, normalized by  $L$ , and figure 4 (b) provides the resulting number of cells, with figure 5 depicting comparison results, figure 6 displaying

DOI: ADD DOINUMBER HERE

the resulting grids for the coarse, medium, and fine meshes (meshes 1, 3, and 5). Grid independence is achieved by medium mesh 3, with the finer mesh 5 deviating only  $\sim 0.12\%$  from this, for an additional  $\sim 49.5\%$  increase in grid elements. In terms of model validation, mesh 3 deviates only  $\sim 10.4\%$  from the experimental measurement of [45]. Mesh 3 data point is highlighted (darker), within Figure 5. Mesh 3 is therefore used for subsequent simulations.

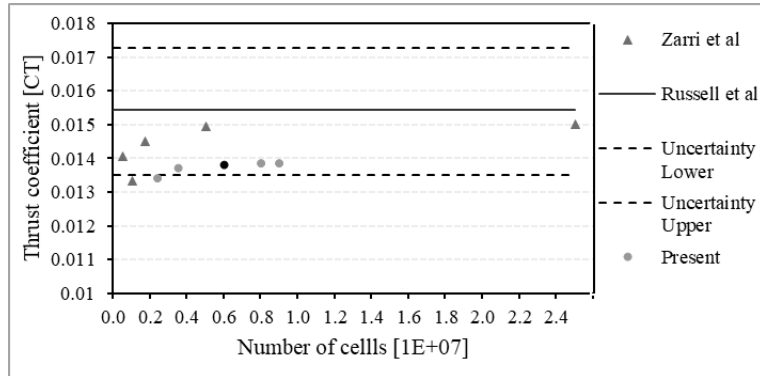


Figure 5- Comparison results of curvature sizing-function study

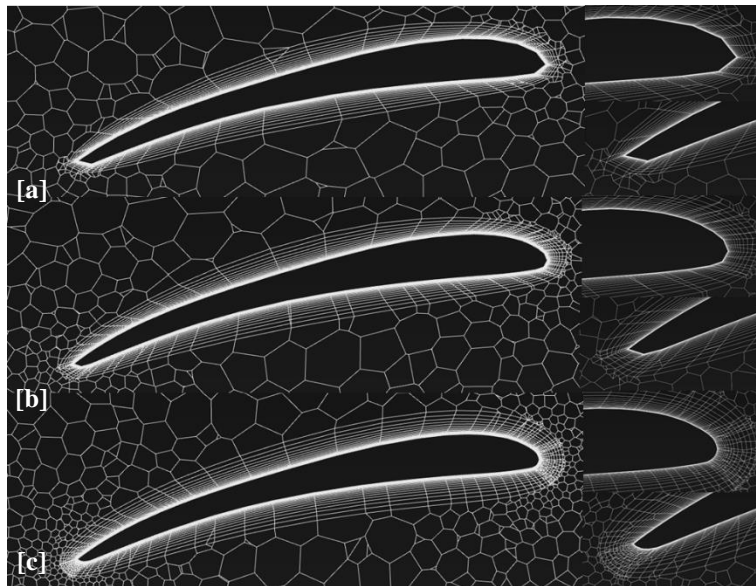


Figure 6- Resulting coarse (a), medium (b), and fine (c) meshes for curvature-function study

### 3.2 Turbulence Effects

To capture smaller-scale flow features for acoustic surface pressures, DES is compared with URANS using  $k - \omega SST$ . Figure 8 displays the time-history of instantaneous thrust produced by the blade, over 0.01s flowtime, or 1 rotation, with data from the 30<sup>th</sup> rotation at 0.3s flowtime. Observing figure 7, DES results have an oscillation of amplitude  $\sim 0.004N$ , with this oscillation pattern shifting upwards towards the second half of the period. The  $k - \omega SST$  experiences an  $\sim 0.001N$  oscillation amplitude, that is shifting downwards slightly towards the end of the period. Figure 8 displays the averaging of  $k - \omega SST$  from the larger force fluctuations present within DES, presumably due to the improved scale-resolving of DES. An interesting point is the smaller sub-oscillations present in the  $k - \omega SST$  time-history, possibly due to the model being limited at the order of modelling below  $1e-4$  resolution and leading to solver instability.

DOI: ADD DOINUMBER HERE

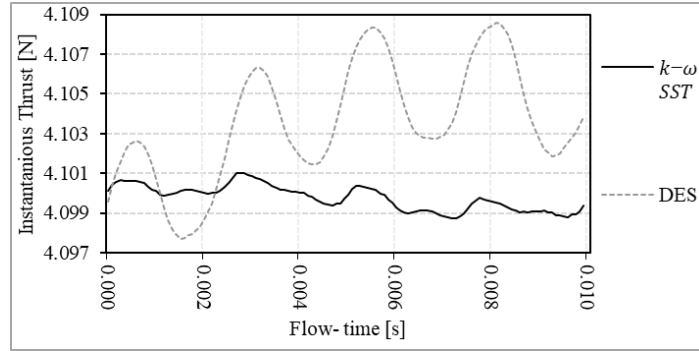


Figure 7- Single-rotor turbulence model comparison results of thrust time-history, over 0.01s flow-time

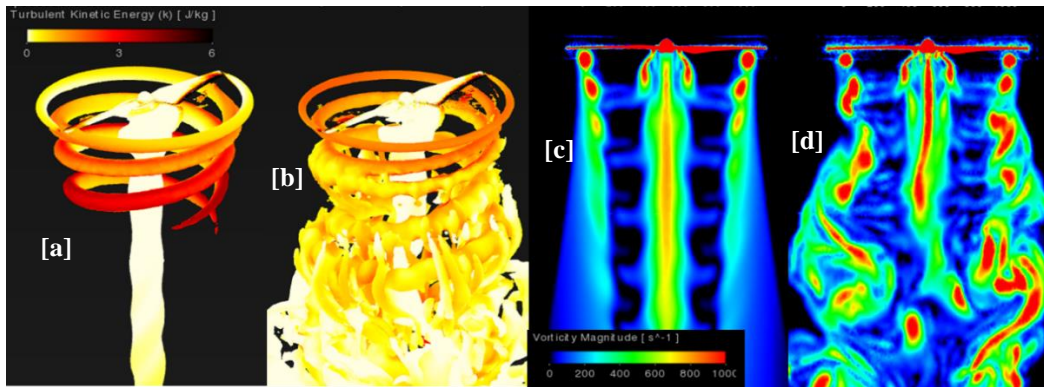


Figure 8-  $k - \omega$  SST (a), and DES (b) raw  $Q$ -criterion iso-surface contours, filtered at  $35000s^{-1}$ , painted with TKE contours at 0.3s flowtime, and  $-\omega$  SST (c), and DES (d) vorticity magnitude contours at 0.3s flowtime.

Figure 8 (a & b) displays raw  $Q$ -criterion iso-surface contours, filtered at  $35000s^{-1}$ , painted with TKE, for  $k - \omega$  SST and DES cases, respectively. Clearly, both figure 8 (a & b) capture the core-wake, in addition to the tip-vortices. The deviation occurs past the approximately third downstream tip-vortex, where figure 8 (a) diffuses off, whereas figure 8 (b) moves into tip-vortex breakdown and core-wake interactions. Figure 8 (c & d) better displays this, with tip-vortex diffusion occurring by the 3<sup>rd</sup> eddy in figure 8 (c) but continuing downstream in figure 8 (d). The comparison depicts the clarity of DES in flow-field prediction, while quantitatively both models provide similar averaged values. All subsequent simulations results were therefore obtained with DES.

### 3.3 Aero-acoustic Validation

#### 3.3.1 Definition

To validate the acoustic prediction capability of ANSYS Fluent, and the current case, an acoustic setup similar to that in [41] is employed. Experimental [45], and Lattice-Boltzmann numerical results [46], of the same case, are also compared. The rotor observer locations employed in [41], translated into ANSYS Fluent, are listed with their coordinates in table 7, where they form an arc of  $7.97 \times D$  (1.905m radius from the blade origin).

Table 6- Present observer location coordinates [m]

| Observer | x-axis | y-axis (rotational axis) | z-axis |
|----------|--------|--------------------------|--------|
| 45°      | 0      | 1.347                    | 1.347  |
| 67.5°    | 0      | 0.729                    | 1.760  |
| 90°      | 0      | 0                        | 1.905  |
| 112.5°   | 0      | -0.729                   | 1.760  |
| 135°     | 0      | -1.347                   | 1.347  |

Sound pressure level (SPL) in dB, is measured to quantitatively judge the acoustic validation. To qualitatively judge the sources, dominant harmonic frequencies are identified; in the case of rotating objects, the Blade Passing Frequencies (BPFs), defined in Equation 2, are compared. The first five BPFs for the present case correspond to the

DOI: ADD DOINUMBER HERE

frequencies of 200, 400, 600, 800, and 1,000 Hz. In Equation 3,  $B$  is the number of blades,  $n$  is the BPF number and  $\Omega$  is the rotation frequency [rad/s].

$$f_{BPF} = B \times n \times \frac{\Omega}{2\pi} \quad (2)$$

### 3.3.2 Source selection

To choose the optimal noise source surface for acoustic far-field predictions, the ‘open’ near-field surface and the rotational domain surface are compared- both act as permeable surfaces, treating the interior rotor source as a quadrupole source [47]. A permeable source is used rather than the blade wall itself due to the noise generation being exterior to the wall surface [47], in addition to capturing the vortical-structure generated noise. This approach is tested and utilised within previous literature [44, 48] based upon the recommendations of [49] who explored the FW-H surface selection in detail. It was found (not shown) that the inner ‘open’ and rotational source surfaces both capture the first five BPFs based on SPL trends, despite some reduction in SPL for the inner ‘open’ source beyond BPF of 2. Comparing extracted BPF SPL values to the literature, figure 9 (a) presents BPF 1 values for all observer locations, while figure 9 (b) presents BPF 2 values. Figure 9 (a) shows almost identical values for both surfaces, where the trend achieved by the literature is followed. Averaging the five observer location SPL values, figure 10 (a) presents deviation from the experimental data [45], where ~15 0% & ~15 3% deviation is obtained for the rotational and inner ‘open’ surfaces, respectively. This appears like Zarri et al.’s [41] deviation, though ~10 0% greater than Thurman et al.’s [46]. Observing figure 10 (b) however, the inner ‘open’ source does not follow the trend for the 45° observer, leading to an ~34 0% deviation from Russell et al.’s [45] data, depicted in figure 10 (b). Observing the rotational source in figure 9 (b), the trend is followed, and corresponding figure 10 (b) deviation is only ~11 0% from [45]. Improved accuracy from the rotational domain source was further evidenced when investigating SPL trends for BPFs 1-5 for observers 90° & 135°. Rotational source SPL is closer to the experimental data for both locations, with averaged deviation across all BPFs of only ~8% & ~18 0%, for 90° & 135°, respectively. The inner ‘open’ source, however, exhibits much higher deviation of ~32 0% & ~42 0% from experimental data for 90° & 135° observer locations, respectively. These findings confirm that the rotational domain best represents the noise source and thus is used in all subsequent simulations.

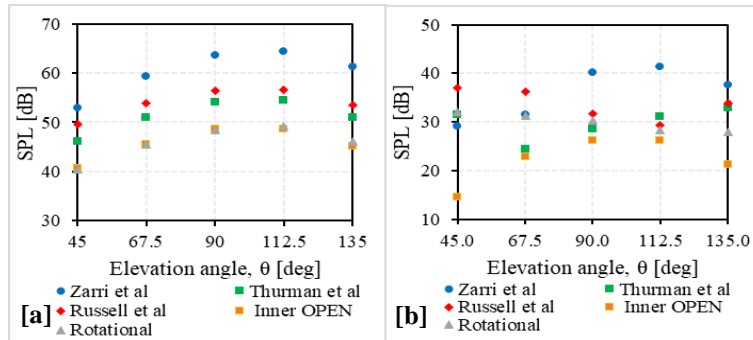


Figure 9- Comparison of SPL against elevation angle for BPF 1 (a) & BPF 2 (b) of the rotational and inner ‘open’ FW-H volume-source-surface contributions.

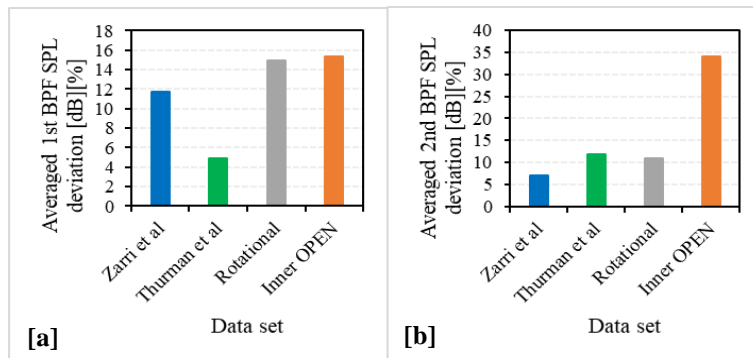


Figure 10- Comparison of averaged SPL deviation from Russell et al. (2016) experimental data for BPF1 (a) & BPF2 (b) of the rotational and inner ‘open’ FW-H volume-source-surface contributions.

DOI: ADD DOINUMBER HERE

### 3.3.3 Temporal Resolution

In terms of achieving accurate temporal resolution, Equation 3 formulates the acoustic Courant Number (CFL), a function of the spatial and temporal CFLs. Achieving a CFL equal to unity implies harmony between spatial and temporal resolution. Table 9 lists the timesteps of interest, with corresponding timestep and CFL details also listed.

$$CFL_{acoustic} = \frac{CFL_{spatial}}{CFL_{temporal}} = \frac{a_0 \times \Delta t}{\Delta x} \quad (3)$$

In Equation 4,  $a_0$  is the speed of sound,  $\Delta t$  is the timestep and  $\Delta x$  is the cell size.

Table 7- Temporal resolution parameters for acoustic setup

| $\Delta t$ [s] | $^\circ\text{rot}/\Delta t$ | $\Delta t$ 's /1rot | Flow- $\Delta t$ 's | Acoustic-source- $\Delta t$ 's | $CFL_{acoustic}$ | $f_{max}$ [Hz] |
|----------------|-----------------------------|---------------------|---------------------|--------------------------------|------------------|----------------|
| 8 33e-5        | 3                           | 120                 | 3600                | 2400                           | ~16              | 6000           |
| 1 39e-4        | 5                           | 72                  | 2160                | 1440                           | ~27              | 3600           |

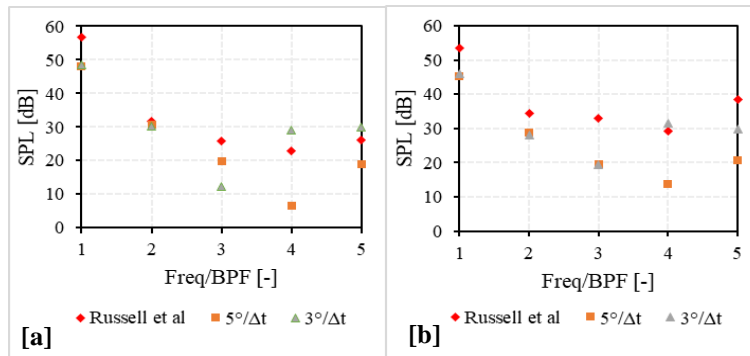


Figure 11- Comparison of SPL against BPF1-5 for 90° (a) & 135° (b) for 5°/Δt & 3°/Δt against experimental data.

Figure 11 (a & b) show a clear trend of almost exact BPF SPL values for BPF 1 & 2, then a deviation where the 3°/Δt SPL tends towards the data [45], whereas the 5°/Δt tends away. Interestingly, 5°/Δt SPL data conforms more to the trend of Russell et al.'s [45] experimental data. Finally, table 10 lists deviation from the data [45], proving improved prediction accuracy with 3°/Δt for both observer locations, as expected from the closer-to-unity  $CFL_{acoustic}$ .

Table 8- Temporal-resolution BPF 1-5 averaged SPL deviation [dB][%] from Russell et al.'s [45] data

| $\Delta t$ [s] | 90° observer | 135° observer |
|----------------|--------------|---------------|
| 3°/Δt          | ~8 1%        | ~17 9%        |
| 5°/Δt          | ~24 1%       | ~32 0%        |

## 4. Finlet design

### 4.1 Design philosophy

Finlets replicate the canopy structures formed by the hairs of owl feathers. Finlet design philosophy is often based upon the designs introduced by Clark et al. [30] for the DU96-W-180 blade aerofoil. Figure 12 displays the baseline designs through idealized versions of Clark et al. [30], with CAD produced by Bolding & Sharma [34]. The finlet design is proving increasingly popular over the rail design, seemingly due to the inherent structural advantage of the finlet compared to rail design, as both were reported to heavily influence surface pressure spectra with noise attenuations up to 30 dB [30].

DOI: ADD DOINUMBER HERE

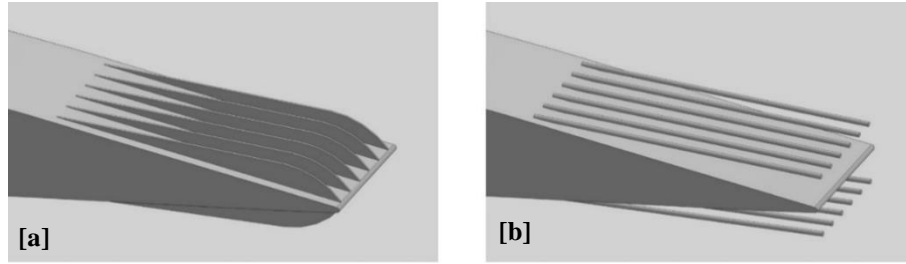


Figure 12- Idealized finlet fence (a), and rail (b) designs, inspired by [30], with CAD produced by [34].

#### 4.1.1 Finlet profile design

The finlet profile from the LE until the maximum height,  $h_f$ , is designed based upon a turbulent boundary layer shape, as introduced in [30], leading to the relation of Equation 4, where a constant,  $\alpha$ , is introduced in [36] to alter the LE profile equation, with  $\alpha$  equating to a value leading to  $h_f$  being reached at half the finlet length,  $l_f$ . Generally, the TE of the finlet design is curved to ease destructive pressure gradients produced in the region when interacting with the TE flow- an example being a TE radius equivalent to  $h_f$ , as reported in [36-37]. Defining essential finlet design parameters, figure 13 displays and label the NACA0012 aerofoil case with finlet treatments produced by [36].

$$y_f \equiv \alpha \times x_f^{4/5} \quad (4)$$

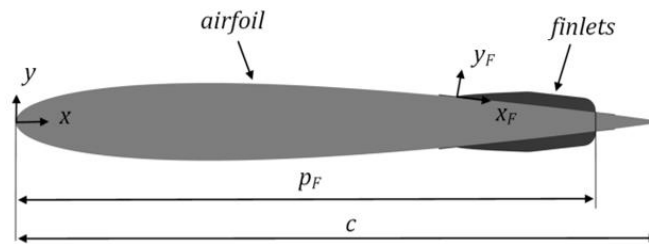


Figure 13- 2-D finlet design schematic applied to a NACA0012 aerofoil [36].

The key finlet design parameters are: chord ( $c$ ), spacing ( $s_F$ ), thickness ( $t_F$ ), local length ( $x_F$ ), local thickness ( $y_F$ ), maximum length ( $l_F$ ), maximum height ( $h_F$ ), and end position ( $p_F$ ).

#### 4.2 Case definition

The current state-of-the-art of finlet design, as discussed in [30-39] relates to aerofoil and/or flat plate studies. For the present work, sizing inspiration from the works [30-33] is applied to the DJI-9450 rotor case. Table 12 summarises the design choices based upon the local blade chord,  $c_{local}$ , with justification of each parameter.

Table 9- Present finlet design choices

| Parameter   | Values (m)                    |                    | Justification   |
|-------------|-------------------------------|--------------------|---|
| $c_{local}$ | At $0.5 \times r/R$<br>0.0227 | At $r/R$<br>0.0106 | Surface treatment applied only from $0.5 \times r/R$ to $r/R$ as predominantly where blade TE-wake reacts.  |
| $Re_x$      | $5.70 \times 10^4$            | $5.33 \times 10^4$ | Calculated for turbulent BL.  |
| $s_F$       | 0.002, 0.004, 0.006           |                    | Observed to be independent of the chord-based Reynolds number in range of $2.5 \times 10^6 \leq Re_x \leq 3 \times 10^6$ [32-33] and $3.87 \times 10^5 \leq Re_x \leq 7.7 \times 10^5$ [30-31]. |
| $t_F$       | 0.0000417                     |                    | Scaled to blade average chord, $c_{avg}$ , through equation 5 and 6 for $t_F$ and $l_F$ respectively.   |
| $l_F$       | 0.00493                       | 0.00231            |   |
| $h_F$       | 0.000780                      | 0.000370           | $h_F/\delta^{99} = 0.5$ to $0.8$ relation recommended [30-33].  |



DOI: ADD DOINUMBER HERE

models were used as those in section 3. The resulting idealized blade grid is almost identical to that of the GrabCAD [40] blade profile, at  $0.5 \times r/R$ , and so is not presented. Mesh metrics are listed in table 13, showing similar quality is achieved through the mesh translation from the GrabCAD [40] onto the idealized model.

Table 10- Idealized mesh translation comparison

| Metric                     | Idealized | GrabCAD [40] |
|----------------------------|-----------|--------------|
| Elements                   | 6254289   | 4619756      |
| Nodes                      | 21043019  | 18268241     |
| Maximum aspect ratio       | 694.38    | 732.64       |
| Minimum orthogonal quality | 0.029     | 0.0392       |

## 5.2 Finlet model on idealised blade

Finlet results employed the exact case as in section 5.1. The resulting finlet-blade mesh is observed and compared in figure 17 to the idealized baseline model profile, at  $0.5 \times r/R$ . Mesh metrics are listed in table 14, showing the base-finlet blade, with  $0.004m s_F$ , achieves similar quality through the mesh translation. The sizing applied yields an average discretization of 55 cells along the finlet edge, with a maximum of 74, and minimum of 36. The mesh for the idealised blade with finlets is shown in figure 16. It is worth noting that for the finlet study only a single blade is considered.

Table 14- Finlet mesh translation comparison

| Metric                     | 0.004 $s_F$ finlets | Idealized baseline |
|----------------------------|---------------------|--------------------|
| Elements                   | 7736909             | 6254289            |
| Nodes                      | 23385702            | 21043019           |
| Maximum aspect ratio       | 606.70              | 694.38             |
| Minimum orthogonal quality | 0.009               | 0.029              |

Comparing the finlet blade aerodynamics to the idealized model, table 15 lists period averaged  $C_T$  values for the 30<sup>th</sup> rotation, at 0.03s flowtime, yielding an  $\sim 0.5\%$  deviation between the two blades. This deviation proves almost negligible, proving the  $0.004 s_F$  finlet blade maintains its aerodynamic performance. Further comparison through pressure coefficient ( $C_p$ ) plots is not presented due to almost negligible difference between the idealized and  $0.004 s_F$  values at  $r/R \times \in \{0.667, 0.833, 0.99\}$ .

Observing effects on the flow-field, specifically paying attention to the region post-finlets, where unsteady surface pressure fluctuations play their part in noise generation, it is observed that the displacing of smaller-scale eddies, through the TKE fluctuations observable in figure 17 (b) within the white box, as opposed to figure 17 (a) is apparent. In the region above the finlet, the TKE is reduced compared with the baseline profile. From figure 17 (c & d), one can see some discrete turbulent blobs in between the finlets. From existing literature, it is possible to postulate that smaller-scale fluctuations are possibly ‘lifted’ above the finlet upper surfaces, as opposed to the larger-scale turbulence seen on the baseline blade. The other mechanism possibly at work is turbulence channelling by the finlets. Both of these mechanisms allow the travelling eddies to avoid interacting with the blade’s trailing edge, thus reduce trailing edge noise generation and scattering. Future work will improve resolution in this region to better display the differences between the baseline design and the finlet design.

Table 15- Finlet blade aerodynamic comparison

|                       | Idealized | 0.004 $s_F$ | Deviation [%] |
|-----------------------|-----------|-------------|---------------|
| Period averaged $C_T$ | 0.0176    | 0.0175      | $\sim 0.5$    |

DOI: ADD DOINUMBER HERE

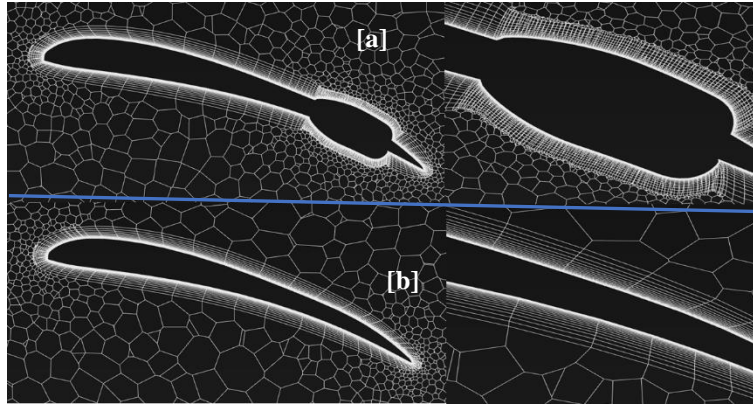


Figure 16- Profile and mesh view at  $0.5 \times r/R$  for the finlet (a) and idealized baseline (b) designs.

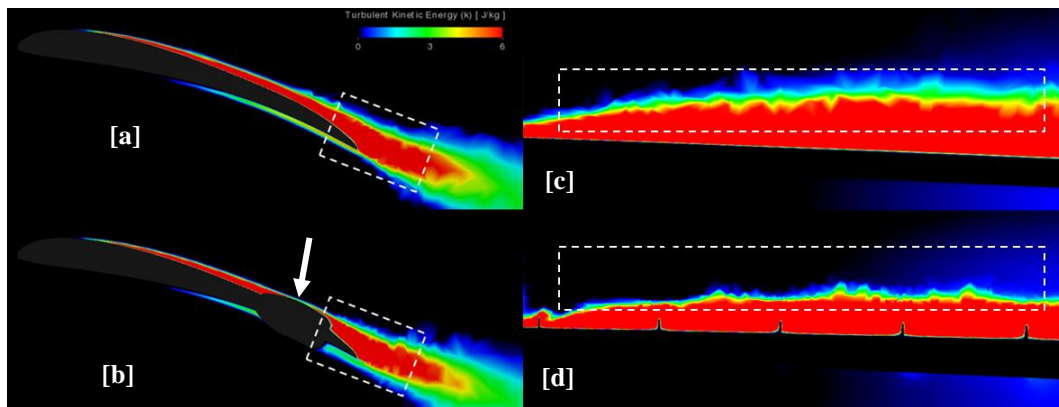


Figure 17- Comparison of idealized and finlet flow, at  $0.5 \times r/R$  (a & b, respectively), through TKE contours, and at  $0.95 > r/R > 0.5$  (c & d, respectively).

## Conclusions

Aerodynamic and aero-acoustic numerical validation and analysis of the DJI-9450 rotor blade has been conducted to provide a numerical framework for subsequent bio-inspired finlet blade design studies. The numerical analysis uses ANSYS Fluent for both flow and aeroacoustic predictions. The simulation framework employs Direct Eddy Simulation (DES) for fluid flow and Ffowcs-Williams-Hawkings acoustic analogy (FW-H) for acoustic data. The averaged  $C_T$  from CFD deviated by  $\sim 11\%$  compared with experimental data. Good agreement was also shown between the present CFD and experiments for SPL values, with the rotational source chosen over the tested inner ‘open’ source, for improved accuracy, deviating  $\sim 15\%$ , &  $\sim 10\%$ , for BPF 1 & 2, respectively. Further analysis on BPF 1-5 for observer locations  $90^\circ$  &  $135^\circ$  revealed an averaged SPL deviation of  $\sim 8\%$ , &  $\sim 18\%$  for the rotational source, for the respective observer locations. To allow ease of modelling the finlets on the blade, the original blade profile was modified such that it has constant twist from mod to blade tip. The effects of finlets on the aerodynamics were shown to be negligible, with an  $\sim 0.5\%$  deviation between the idealized model, and the 0.004  $s_F$  finlet blade. The finlets exhibit a reduced TKE compared with the baseline design. Turbulence ‘lifting’ of smaller-scale eddies and turbulence channelling, both known to be sources of noise reduction for surfaces with finlets, may be at play when finlets are added. With negligible effects on aerodynamics and turbulence lifting/channelling occurring with finlet design, this technology demonstrates its potential for noise reduction on UAV blades. The framework provides a useful, easy to use tool for noise-optimisation studies of finlet designs.

## Recommendations For Future Work

To improve current simulation results, a few research directions can be explored. Focus should be on reducing the order of near-field mesh resolution to reduce pressure fluctuation diffusion into near-field mesh, for acoustic source-surface purposes to test FW-H surface contributions more fairly. In addition, it is important to understand which surface is most effective at capturing the noise source, adding to existing work on surface selection [49]. Future focus should also be on capturing smaller-scale finlet induced flow phenomena and evaluating their effects more thoroughly.

DOI: ADD DOINUMBER HERE

More work is needed to complete the aero-acoustic analysis and comparison of the finlet blade, with a shift then to conducting in-depth aerodynamic and aero-acoustic analysis of the different finlet geometric parameters to observe their effects. Although creating an idealised blade profile with constant twist from mid to blade tip was a useful solution for finlets implementation, techniques such as overset mesh should be explored so that a real UAV blade profile is not altered when finlets are placed on it. Additionally, applying all these future works to multi-rotor configurations, looking into the interactional effects when finlets are applied, say, to a quadcopter UAV with two bladed rotors.

## References

- [1] R. Merkert and J. Bushell, "Managing the drone revolution: A systematic literature review into the current use of airborne drones and future strategic directions for their effective control," *J Air Transp Manag*, vol. 89, p. 101929, 2020, doi: <https://doi.org/10.1016/j.jairtraman.2020.101929>.
- [2] J. M. Robinson, P. A. Harrison, S. Mavoa, and M. F. Breed, "Existing and emerging uses of drones in restoration ecology," *Methods Ecol Evol*, vol. 13, no. 9, pp. 1899–1911, Sep. 2022, doi: <https://doi.org/10.1111/2041-210X.13912>.
- [3] NASA Langley Research Centre, "Turbulence Modeling Resource- 2DN00: 2D NACA 0012 Airfoil Validation Case.," Aug. 28, 2020. [https://turbmodels.larc.nasa.gov/naca0012\\_val.html](https://turbmodels.larc.nasa.gov/naca0012_val.html)
- [4] A. N. Kusyumov, S. A. Mikhailov, L. I. Garipova, A. S. Batrakov, and G. Barakos, "Prediction of helicopter rotor noise in hover," *EFM14 – Experimental Fluid Mechanics 2014*, vol. 92, no. 02042, pp. 0–5, 2015.
- [5] A. F. Deming, "Noise from propellers with symmetrical sections at zero blade angle, II," Dec. 1938. Accessed: Dec. 01, 2022. [Online]. Available: <https://ntrs.nasa.gov/citations/19930081438>
- [6] K. S. Brentner and F. Farassat, "Modeling aerodynamically generated sound of helicopter rotors," *Progress in Aerospace Sciences*, vol. 39, no. 2, pp. 83–120, 2003, doi: [https://doi.org/10.1016/S0376-0421\(02\)00068-4](https://doi.org/10.1016/S0376-0421(02)00068-4).
- [7] ANSYS, "Chapter 11: Aerodynamically Generated Noise," in *ANSYS Fluent Theory Guide*, 2022, pp. 407–422.
- [8] E. Pang, A. Cambray, D. Rezgui, M. Azarpeyvand, and S. showkat ali, *Investigation Towards a Better Understanding of Noise Generation from UAV Propellers*. 2018. doi: 10.2514/6.2018-3450.
- [9] J. Nixon and S. Dance, "The Sound of the Drone Uprising – Aeroacoustics of Drone Blades," in *Quiet Drones*. Paris 17 - 21 Oct 2020, Paris, 2020, pp. 1–8. Accessed: Nov. 17, 2022. [Online]. Available: <https://openresearch.lsbu.ac.uk/item/8v1w5>
- [10] T. Chong and A. Vathylakis, "On the aeroacoustic and flow structures developed on a flat plate with a serrated sawtooth trailing edge," *J Sound Vib*, vol. 354, pp. 65–90, Oct. 2015, doi: 10.1016/j.jsv.2015.05.019.
- [11] F. Avallone, W. C. P. van der Velden, D. Ragni, and D. Casalino, "Noise reduction mechanisms of sawtooth and combed-sawtooth trailing-edge serrations," *J Fluid Mech*, vol. 848, pp. 560–591, 2018, doi: 10.1017/jfm.2018.377.
- [12] S. K. Singh and S. Narayanan, "Control of airfoil broadband noise through non-uniform sinusoidal trailing-edge serrations," *Physics of Fluids*, vol. 35, no. 2, p. 025139, Feb. 2023, doi: 10.1063/5.0133556.
- [13] Z. Ning and H. Hu, *An Experimental Study on the Aerodynamics and Aeroacoustic Characteristics of Small Propellers*. 2017. doi: 10.2514/6.2016-1785.
- [14] N. Intravartolo, T. C. Sorrells, N. Ashkharian, and R. Kim, "Attenuation of Vortex Noise Generated by UAV Propellers at Low Reynolds Numbers," 2017. Accessed: Feb. 16, 2023. [Online]. Available: <https://www.semanticscholar.org/paper/Attenuation-of-Vortex-Noise-Generated-by-UAV-at-Low-Intravartolo-Sorrells/e9b8a8ebaa82ccb3fb21c9043993780c2c3012f3>
- [15] T. Pagliaroli, R. Camussi, P. Candeloro, O. Giannini, G. Bella, and R. Panciroli, *Aeroacoustic Study of small scale Rotors for mini Drone Propulsion: Serrated Trailing Edge Effect*. 2018. doi: 10.2514/6.2018-3449.
- [16] P. Candeloro, R. E. Nargi, F. Patané, and T. Pagliaroli, "Experimental Analysis of Small-Scale Rotors with Serrated Trailing Edge for Quiet Drone Propulsion," *J Phys Conf Ser*, vol. 1589, 2020, Accessed: Feb. 16, 2023. [Online]. Available: <https://www.semanticscholar.org/paper/Experimental-Analysis-of-Small-Scale-Rotors-with-Candeloro-Nargi/3abed7f78b5f87a79ba76c82fa31a6158a474737>
- [17] P. Candeloro, R. E. Nargi, E. Grande, D. Ragni, and T. Pagliaroli, "Experimental Fluid Dynamic Characterization of Serrated Rotors for Drone Propulsion," *J Phys Conf Ser*, vol. 1977, no. 1, p. 012007, 2021, doi: 10.1088/1742-6596/1977/1/012007.
- [18] S. M. Hasheminejad, T. Chong, P. Joseph, and G. Lacagnina, *Airfoil Self-Noise Reduction Using Fractal-Serrated Trailing Edge*. 2018. doi: 10.2514/6.2018-3132.
- [19] D. Ragni, F. Avallone, W. van der Velden, and D. Casalino, "Measurements of near-wall pressure fluctuations for trailing-edge serrations and slits," *Exp Fluids*, vol. 60, Nov. 2018, doi: 10.1007/s00348-018-2654-5.
- [20] C. Arce León, R. Merino-Martínez, D. Ragni, F. Avallone, and M. Snellen, "Boundary layer characterization and acoustic measurements of flow-aligned trailing edge serrations," *Exp Fluids*, vol. 57, no. 12, p. 182, 2016, doi: 10.1007/s00348-016-2272-z.
- [21] Y. Hong, D. Han, and K. Yee, "DESIGN PARAMETER STUDY OF DRONE BLADE CONSIDERING AEROACOUSTICS," in *31st Congress of the International Council of the Aeronautical Sciences*, September 09-14, Belo Horizonte, 2018, pp. 1–8. Accessed: Nov. 03, 2022. [Online]. Available: [https://icas.org/ICAS\\_ARCHIVE/ICAS2018/data/papers/ICAS2018\\_0216\\_paper.pdf](https://icas.org/ICAS_ARCHIVE/ICAS2018/data/papers/ICAS2018_0216_paper.pdf)
- [22] Y. Wei, F. Xu, S. Bian, and D. Kong, "Noise Reduction of UAV Using Biomimetic Propellers with Varied Morphologies Leading-edge Serration," *J Bionic Eng*, vol. 17, no. 4, pp. 767–779, 2020, doi: 10.1007/s42235-020-0054-z.

DOI: ADD DOINUMBER HERE

- [23] P. Chaitanya, S. Narayanan, J. Phillip, and K. Jae, “Leading edge serration geometries for significantly enhanced leading edge noise reductions,” *Apr.* 2016. doi: 10.2514/6.2016-2736.
- [24] P. Chaitanya et al., “Performance and mechanism of sinusoidal leading edge serrations for the reduction of turbulence–aerofoil interaction noise,” *J Fluid Mech.*, vol. 818, pp. 435–464, 2017, doi: DOI: 10.1017/jfm.2017.141.
- [25] S. Narayanan, P. Chaitanya, S. Haeri, P. Joseph, J. W. Kim, and C. Polacsek, “Airfoil noise reductions through leading edge serrations,” *Physics of Fluids*, vol. 27, no. 2, p. 025109, Feb. 2015, doi: 10.1063/1.4907798.
- [26] P. Candeloro, D. Ragni, and T. Pagliaroli, “Small-Scale Rotor Aeroacoustics for Drone Propulsion: A Review of Noise Sources and Control Strategies,” *Fluids*, vol. 7, no. 8, 2022, doi: 10.3390/fluids7080279.
- [27] F. Moslem, M. Masdari, K. Fedir, and B. Moslem, “Experimental investigation into the aerodynamic and aeroacoustic performance of bioinspired small-scale propeller planforms,” *Proc Inst Mech Eng G J Aerosp Eng*, vol. 237, pp. 75–90, 2022, Accessed: Feb. 18, 2023. [Online]. Available: <https://www.semanticscholar.org/paper/Experimental-investigation-into-the-aerodynamic-and-Moslem-Masdari/c599c5138cbd00185eb90df00148b1fc08706fb7>
- [28] R. M. Ariefianto, R. N. Hasanah, Wijono, and R. A. Aprilianto, “Performance Investigation of a Humpback Whale-Inspired Vertical Axis Current Turbine,” in *Proceedings of the International Conference on Sustainable Environment, Agriculture and Tourism (ICOSEAT 2022)*, Atlantis Press, 2022, pp. 749–758. doi: 10.2991/978-94-6463-086-2\_99.
- [29] L. Wang, X. Liu, L. Wu, and D. Li, “Effect of the asymmetric bio-inspired trailing-edge serrations on sound suppression in a coupled owl-based airfoil,” *Applied Acoustics*, vol. 191, p. 108667, 2022, doi: <https://doi.org/10.1016/j.apacoust.2022.108667>.
- [30] I. Clark, W. J. Devenport, J. Jaworski, C. Daly, N. Peake, and S. A. Glegg, “The Noise Generating and Suppressing Characteristics of Bio-Inspired Rough Surfaces,” in *20th AIAA/CEAS Aeroacoustics Conference*, in *AIAA AVIATION Forum. American Institute of Aeronautics and Astronautics*, 2014. doi: doi:10.2514/6.2014-2911.
- [31] I. A. Clark et al., “Bioinspired Trailing-Edge Noise Control,” *AIAA Journal*, vol. 55, no. 3, pp. 740–754, Dec. 2016, doi: 10.2514/1.J055243.
- [32] A. Afshari, M. Azarpeyvand, A. A. Dehghan, and M. Szóke, *Trailing Edge Noise Reduction Using Novel Surface Treatments*. 2016. doi: 10.2514/6.2016-2834.
- [33] A. Afshari, M. Azarpeyvand, A. A. Dehghan, M. Szóke, and R. Maryami, “Trailing-edge flow manipulation using streamwise finlets,” *J Fluid Mech.*, vol. 870, pp. 617–650, 2019, Accessed: Feb. 18, 2023. [Online]. Available: <https://www.semanticscholar.org/paper/Trailing-edge-flow-manipulation-using-streamwise-Afshari-Azarpeyvand/1759592d5202521d9fd84fae988801dada0299d6>
- [34] A. Bodling and A. Sharma, “Numerical investigation of noise reduction mechanisms in a bio-inspired airfoil,” *J Sound Vib.*, vol. 453, pp. 314–327, 2019, doi: <https://doi.org/10.1016/j.jsv.2019.02.004>.
- [35] Y. Shi and S. Lee, “Numerical study of 3-D finlets using Reynolds-averaged Navier–Stokes computational fluid dynamics for trailing edge noise reduction,” *Int J Aeroacoust.*, vol. 19, no. 1–2, pp. 95–118, Mar. 2020, doi: 10.1177/1475472X20905053.
- [36] F. Gstrein, N. Zang, and M. Azarpeyvand, “Application of Finlets for Trailing Edge Noise Reduction of a NACA 0012 Airfoil,” in *AIAA AVIATION 2020 FORUM*, in *AIAA AVIATION Forum. American Institute of Aeronautics and Astronautics*, 2020. doi: doi:10.2514/6.2020-2502.
- [37] F. Gstrein, B. Zang, Y. D. Mayer, and M. Azarpeyvand, “Airfoil Trailing-Edge Noise Reduction by Application of Finlets,” *AIAA Journal*, vol. 60, no. 1, pp. 236–248, Sep. 2021, doi: 10.2514/1.J060699.
- [38] S. Palani et al., *Comparison of finlet rails and fences for trailing edge noise reduction in NACA0012 aerofoil*. 2022. doi: 10.2514/6.2022-3015.
- [39] V. B. Ananthan and R. A. D. Akkermans, “Trailing edge noise reduction using bio-inspired finlets,” *J Sound Vib.*, vol. 549, p. 117553, 2023, doi: <https://doi.org/10.1016/j.jsv.2023.117553>.
- [40] “DJI-Phantom 3 DJI-9450 Rotor.” Accessed: Jan. 05, 2023. [Online]. Available: <https://grabcad.com/library/phantom-3-prop-1>
- [41] A. Zarri, E. Dell’Erba, W. Munters, and C. Schram, “Aeroacoustic installation effects in multi-rotorcraft: Numerical investigations of a small-size drone model,” *Aerosp Sci Technol.*, vol. 128, p. 107762, Sep. 2022, doi: 10.1016/J.AST.2022.107762.
- [42] ANSYS, “Chapter 10: Modeling Flows with Moving Reference Frames,” in *ANSYS Fluent Users Guide*, 2022, pp. 1661–1678.
- [43] R. R. Mankbadi, S. O. Afari, and V. V Golubev, “High-Fidelity Simulations of Noise Generation in a Propeller-Driven Unmanned Aerial Vehicle,” *AIAA Journal*, vol. 59, no. 3, pp. 1020–1039, Dec. 2020, doi: 10.2514/1.J059117.
- [44] TCAE, “Acoustic Benchmark Propeller DJI-9450.” Accessed: Dec. 10, 2022. [Online]. Available: <https://www.cfdsupport.com/acoustic-benchmark-propeller-dji-9450.html>
- [45] C. Russell, J. Jung, G. Willink, and B. Glasner, “Wind Tunnel and Hover Performance Test Results for Multicopter UAS Vehicles,” in *American Helicopter Society (AHS) International Annual Forum and Technology Display*, May 2016, pp. 1–20. Accessed: Oct. 17, 2022. [Online]. Available: <https://ntrs.nasa.gov/citations/20160007399>
- [46] C. S. Thurman, N. S. Zawodny, and J. S. Baeder, “Computational Prediction of Broadband Noise from a Representative Unmanned Aerial System Rotor,” in *76th Annual Forum & Technology Display*, Virginia Beach, VA, Jun. 2020, pp. 1–9. Accessed: Apr. 23, 2023. [Online]. Available: <https://ntrs.nasa.gov/citations/20205003566>
- [47] ANSYS, “Chapter 19: Predicting Aerodynamically Generated Noise,” in *ANSYS Fluent Users Guide*, 2022, pp. 2417–2465.

DOI: ADD DOINUMBER HERE

- [48] S. O. Afari and R. R. Mankbadi, "Simulations of multi-rotor interaction noise at hovering & forward flight conditions," *Int J Aeroacoust*, vol. 0, no. 0, p. 1475472X231152608, Jan. 2023, doi: 10.1177/1475472X231152608.
- [49] L. Lopes, D. Jr, D. Nark, and K. Wiedemann, *Identification of Spurious Signals from Permeable Ffowcs Williams and Hawkings Surfaces*. 2017.